PLANETARY SCIENCE

Radiogenic heating sustains long-lived volcanism and magnetic dynamos in super-Earths

Haiyang Luo¹*, Joseph G. O'Rourke², Jie Deng¹*

Radiogenic heat production is fundamental to the energy budget of planets. Roughly half of the heat that Earth loses through its surface today comes from the three long-lived, heat-producing elements (potassium, thorium, and uranium). These three elements have long been believed to be highly lithophile and thus concentrate in the mantle of rocky planets. However, our study shows that they all become siderophile under the pressure and temperature conditions relevant to the core formation of large rocky planets dubbed super-Earths. Mantle convection in super-Earths is then primarily driven by heating from the core rather than by a mix of internal heating and cooling from above as in Earth. Partitioning these sources of radiogenic heat into the core remarkably increases the core-mantle boundary (CMB) temperature and the total heat flow across the CMB in super-Earths. Consequently, super-Earths are likely to host long-lived volcanism and strong magnetic dynamos.

Copyright © 2024 me Authors, some rights reserved; exclusive licensee American Association for the Advancement of Science. No claim to original U.S.
Government Works.
Distributed under a Creative Commons Attribution License 4.0 (CC BY).

INTRODUCTION

With more than 5000 confirmed exoplanets, including the commonly found super-Earths that are ~1 to 5 times the mass of Earth and possibly have core-mantle structures like Earth's (1-3), the pursuit of Earth-like habitable planets (4-6) beyond our solar system remains a compelling subject of exploration. Two critical factors that determine a planet's habitability are mantle degassing via volcanism, which can support a global volatile cycle necessary to maintain surface habitability (7, 8), and the magnetic field, which can shield the planet's atmosphere from the solar wind of its host star and protect its surface from high-energy charged particles (9). Active volcanism requires partial melting of mantle rock. Magnetic fields, using Earth as an example, are maintained by vigorous convection in the outer core, known as the geodynamo, and are governed by the heat flow across the core-mantle boundary (CMB) (10). The generation and sustenance of volcanism (11-15) and magnetic fields (16-21) in super-Earths are under debate because constraining the thermal evolution of exoplanets remains challenging (22).

A fundamental factor determining the existence of volcanism and magnetic fields is radiogenic heat production, which contributes to the overall heat budget of a planet and profoundly affects the temperature and dynamical properties of the core and mantle (23). In the Earth's present-day mantle, the heat budget consists of secular cooling, heat flow from the core, and radiogenic heat production from three long-lived elements: potassium (K), thorium (Th), and uranium (U). These heat-producing elements (HPEs) account for almost half of the Earth's total surface heat flow (24). Today, roughly one-third of the total radiogenic heat production is sequestered in the crust and upper mantle (24) because K, Th, and U are incompatible in silicate melt and are thus extracted from the convecting mantle by crustal production. In comparison, radiogenic heating in the core is typically discounted because HPEs are assumed to be highly lithophile (rock loving). Studies of exoplanets have assumed that HPEs always remain lithophile, even in super-Earths of larger sizes. This assumption stems from experimental (25-30) and computational (31, 32) studies that have only investigated element partitioning in relation to Earth.

However, it is not clear whether HPEs are still lithophile under extreme pressure (up to \sim 1400 GPa) and temperature (up to \sim 14,000 K) conditions relevant to super-Earths. Previous studies (30, 33, 34) revealed that some lithophile elements (e.g., B, Mg, Cl, and K) become less lithophile (more siderophile and iron loving) as pressure and temperature increase. Whether this shift toward siderophile behavior persists up to ~10 times larger pressures at the conditions of super-Earths is unknown, given the induced possibly marked structural changes of metal and silicate. For example, in silicate, the coordination number of Si with respect to O may increase from about 6 to 8 and intrinsically disordered phase may emerge (35). The metalsilicate partition coefficients of some other lithophile elements (e.g., F and P) show no notable changes with increasing pressure (>~20 GPa) and temperature (34, 36). Should HPEs become siderophile and present in substantial proportions within the core, the generation and evolution of volcanism and magnetic dynamos in super-Earths would deviate from predictions outlined in existing models.

In this study, we used ab initio molecular dynamics (AIMD) simulations and the thermodynamic integration method to calculate the partition coefficients of K, Th, and U between metal and silicate melt (tables S1 and S2). These three elements are assumed to exist nominally as K₂O, ThO, ThO₂, UO, and UO₂. By determining the chemical potentials of the five species in metal and silicate melts (figs. S1 and S2) and calculating their differences, we obtained the partition coefficients (Materials and Methods). Initially, we compared the partition coefficients of K₂O in Fe-MgSiO₃ and Fe_{5.4}O (Fe with 5.0 wt % O)-MgSiO₃ systems and found that adding 5 wt % oxygen to the iron core does not change the K2O partitioning notably (fig. S3). We then calculated the partition coefficients of K₂O, ThO, ThO₂, UO, and UO₂ between Fe_{5.4}O and MgSiO₃ at 50, 135, 500, and 1000 GPa, corresponding to 3500, 5000, 9000, and 13,000 K, respectively. The assumed equilibration temperatures are near the estimated silicate liquidus at those pressures (37) and guarantee the liquid state of all our simulations.

In super-Earths, core formation should occur in tandem with planetary accretion, which features metal-silicate equilibration over a wide range of pressure/temperature conditions (37). However, simplified, single-stage models can reproduce the size and density of Earth's core plus the abundances of several moderately siderophile elements in the mantle (38–40). Multistage models are more realistic (38, 41, 42),

¹Department of Geosciences, Princeton University, Princeton, NJ, USA. ²School of Earth and Space Exploration, Arizona State University, Tempe, AZ, USA.

^{*}Corresponding author. Email: haiyang.luo@princeton.edu (H.L.); jie.deng@princeton.edu (J.D.)

but the evolution of pressure, temperature, and redox conditions during accretion is difficult (perhaps impossible) to determine for exoplanets. Applied to Earth, the best-fit pressure/temperature conditions are ~55 GPa and ~3400 K in single-stage models (38, 40, 43), that is, near the silicate liquidus temperature at mid-mantle pressures. Single-stage models may likewise predict the abundances of HPEs in the cores and mantles of exoplanets. Here, we assume equilibration pressures of 50, 135, and 500 GPa for super-Earths with masses of ~1, 2 to 3, and 4 to 6 Earth masses ($M_{\rm E}$), respectively, because these pressures are representative of the middle-to-lower mantles of such exoplanets, which may melt during accretion even in the absence of late giant impacts (20, 44, 45). Increasing pressure and temperature may lead to more Mg, Si, and O atoms dissolved into the liquid metal and more Fe present in the silicate melt. Fe_{5.4}O and MgSiO₃ are used to represent the liquid metal and silicate melt, as we found that varying the compositions of liquid metal and silicate melt in a wide range (e.g., from Fe₅₄O₁₁K₂ to Fe₇₂Mg₃Si₁₆O₁₆K₁ and from MgSiO₃ to Ca₂Mg₃₀Fe₄Al₂Si₂₄O₈₇) does not notably change the characteristics of the local structure of K/Th/U with respect to Fe/O (figs. S4 and S5). We performed two-phase molecular dynamics simulations of K-bearing metal-silicate coexistence (fig. S6). The consistency in the results between two-phase simulations and thermodynamic integration also indicates that Fe_{5.4}O and MgSiO₃ are acceptable choices for simplifying the metal and silicate compositions, respectively, when calculating the partition coefficients of K, Th, and U. In addition, the calculated chemical potentials of K₂O and UO with more complex compositions (Fe₅₄Mg₁Si₃O₁₀ and Ca₂Mg₃₀Fe₄Al₂Si₂₄O₈₇) are comparable to those in Fe_{5.4}O and MgSiO₃ (tables S3 and S4).

RESULTS AND DISCUSSION

The metal-silicate partition coefficients that we calculated for K_2O_3 ThO₂, and UO₂ at 50 GPa are in good agreement with experimental data (Fig. 1) (30), validating the compositions of metal and silicate that we adopted as well. The experiments suggested that U likely exists in the 2+ oxidation state in silicate melts around 50 GPa. This inferred oxidation state assumes that U is reduced to a zerooxidation state in liquid iron. However, we find that U still strongly interacts with oxygen in liquid iron alloys and is likely in the 2+ oxidation state in liquid iron alloys according to Bader charge analysis (table S5). The electron localization functions (fig. S7) and projected densities of states (figs. S8 and S9) also reveal that U and Th strongly interact with oxygen in liquid iron alloys at 50 GPa (to a less extent for K), although these interactions weaken with pressure. As pressure rises, we observe an upward trend in the partition coefficients of the three heat producing elements, indicating a greater affinity for the metal phase. It is important to note that the degree of increase varies between the elements. Specifically, the metal-silicate partition coefficient of K_2O increases from $0.0012^{+0.0073}_{-0.0010}$ at 50 GPa to $5.4^{+3.0}_{-1.9}$ at 1000 GPa. In comparison, the corresponding partition coefficients of ThO₂ and UO₂ rise from $0.00081^{+0.00367}_{-0.00066}$ to 1337^{+466}_{-346} and from $0.35^{+1.66}_{-0.29}$ to 813^{+289}_{-213} , respectively. Although the Bader charges of Th and U are found to decrease with increasing pressure (table S5), implying that the cases of ThO and UO may be more realistic at 500 and 1000 GPa, the differences in the partition coefficients between ThO₂ and ThO (or UO₂ and UO) are relatively small (~0.5 log unit). On the basis of our results, we estimated the initial distributions of the heat-producing radionuclides (40K, 232Th, 235U, and ²³⁸U) between core and mantle in super-Earths using the galactic

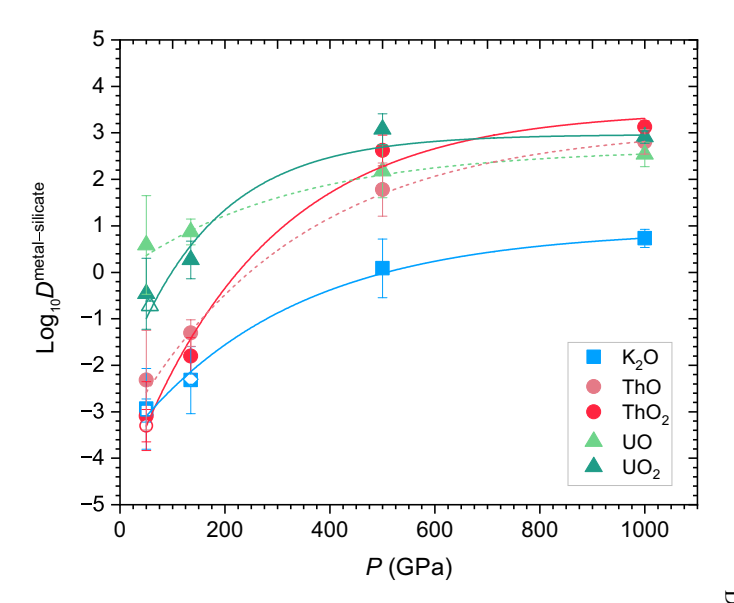


Fig. 1. Partition coefficients of K, Th, and U. Calculated partition coefficients of K_2O , ThO, ThO₂, UO, and UO₂ between metal (Fe with 5.0 wt % O) and silicate (MgSiO₃) melts as a function of pressure (*P*). Partition coefficients are calculated using mole fractions. Solid symbols are our computational results. The corresponding open symbols represent experimental data (30) obtained at relatively low oxygen fugacity (IW–2, corresponding to 2 log(fO_2) units below the iron-wüstite buffer). The open diamond symbol is the previous computational result of K_2O (31). The experimental data acquired under lower pressures (~1 to 6 GPa) are not shown here, as the notable structural change of silicate melt within this pressure range may influence the partitioning behavior of elements in a manner that differs from the trend observed at higher pressures (103). Lines connecting computational results are best fit for K_2O (blue solid), ThO (light red dashed), ThO₂ (red solid), UO (light green dashed), and UO₂ (dark green solid).

chemical evolution model (46). Table 1 shows that the abundances of radionuclides in the core and mantle vary markedly with the pressure and temperature conditions of core-mantle differentiation, as a result of the change in their partitioning behaviors. For example, when 40 K transitions from a lithophile element at 135 GPa (e.g., at 20 C to 3 $M_{\rm E}$) to a siderophile element at 500 GPa (20 C 20 C 20 C), its abundance in the core increases from 2.2 to 359 parts per billion. Note that the abundances of 232 Th, 235 U, and 238 U remain relatively stable between 500 and 1000 GPa (e.g., 24 M_E), because their partition coefficients at 500 GPa are already large enough to retain most of these radionuclides in the core.

Our partition coefficients imply that super-Earths have markedly different heat budgets compared to Earth. We used parameterized models to determine how concentrating HPEs in the core affects planetary evolution (Materials and Methods). These models were not designed to reproduce individual planets. Instead, they illustrate the magnitudes and directions of effects on key processes, including near-surface melt production and dynamo activity. We modeled super-Earths with whole-mantle convection in the stagnant-lid regime and masses $\leq 6~M_{\rm E}$ (fig. S4). Our models are not applicable for more massive super-Earths. Whole-mantle convection is less likely in super-Earths with masses above $\sim 6~M_{\rm E}$ as adiabatic compression leads to convective stability in the shallow mantle (47, 48). Deep within super-Earths of $>6~M_{\rm E}$, silicates and metal may also become miscible at temperatures $>10^4~{\rm K}$, blurring the boundary between core and mantle. In each model, we tracked the potential temperature of

Nuclide abundances (ppb)	Pressure/temperature of core-mantle equilibration (GPa/K)			
	50/3500	135/5000	500/9000	1000/13,000
Mantle				
⁴⁰ K	463.3	462.4	292.1	128.9
²³⁵ U	14.05	8.673	0.223	0.098
²³⁸ U	53.42	32.97	0.849	0.374
²³² Th	154.9	153.8	5.174	0.501
Core		•	•	
⁴⁰ K	0.542	2.237	359.2	701.3
²³⁵ U	4.917	16.19	33.90	34.16
²³⁸ U	18.69	61.54	128.9	129.9
²³² Th	0.127	2.461	313.9	323.7

the mantle (T_P) and the temperature of the core (T_C) . We calculated the heat fluxes out of the mantle from conduction $(Q_{M,cond})$ and melt production $(Q_{M,melt})$. Using the initial abundances from Table 1, we computed the rates of heat production in the mantle (H_M) and core (H_C) . Melt production sequesters HPEs from the mantle into the lithosphere (H_L) in these models, which do not include a separate crust. The heat flux from the core (Q_C) determines how fast the core cools, when the inner core nucleates, and whether convection is vigorous enough to generate a dynamo (45).

Figure 2 shows snapshots of the evolution of a $4-M_E$ super-Earth at 4.5 billion years (Gyr) in our models. Both models start with the same initial temperatures and total amounts of internal heating. Figure 2A is the result of the partition coefficients from this study at 500 GPa and 9000 K, while Fig. 2B represents the conventional assumption that HPEs are lithophile. Our results imply that heat from the core drives mantle convection in super-Earths, with a near-zero Urey ratio (49). In contrast, the conventional model implies that internal heating is the most important heat source for mantle convection, with Urey ratios >0.50. Because the lithospheric viscosity is strongly temperature dependent, the mantle self-regulates in either case to a potential temperature of ~1800 K at 4.5 Gyr with ~140 to 150 km³ of melt production per year near the surface. If $H_C \sim 0$, then our models predict that the inner core grows to >2100 km by 4.5 Gyr. However, sequestering HPEs into the core makes the core hotter by >1000 K at 4.5 Gyr. Because radiogenic heating and inner core growth trade-off in the dissipation budget for the dynamo (45), both models predict a (dominantly dipolar) dynamo with a field strength of ~60 to 65 mT at the equator. However, the model with siderophile HPEs has relatively longer-lived magmatic (by ~1 Gyr or >13%) and magnetic activity (by ~8 Gyr or >87%).

Beyond the fundamental change on how mantle convection is powered, our results indicate that super-Earths can sustain volcanism and magnetic fields for much longer timespans than previously believed (18, 45). Figure 3 illustrates the calculated lifetimes of melt production and dynamos for stagnant-lid planets with masses of 1 to 6 $M_{\rm E}$. Here, we used three formulations for the viscosity of the lower mantle that were based on studies of post-perovskite (50, 51), the mineral phase that likely dominates the lower mantles of super-Earths of $<4\,M_{\rm E}$. Other phases likely dominate the lower mantles of more massive super-Earths. Because the properties of super-Earths

are uncertain, we tested the effects of varying viscosity by over ~10 orders of magnitude, which did not change our primary conclusions. As predicted by previous studies (18, 45), we find that larger planets can produce longer-lived volcanism and magnetism, basically because of the cubic versus square scaling of volume and surface area with planetary radius. Lower viscosities in the basal mantle cause higher heat flow from the core, as expected, in turn, leading to more volcanism and stronger dynamos. Critically, our result is that partitioning HPEs into the core keeps the core hotter over geologic time while also maintaining a high heat flux into the basal mantle. Depending on the viscosity of the lower mantle, HPEs in the cores of $>4-M_{\rm E}$ super-Earths can increase, by >50 to 100%, the durations of near-surface melting and magnetism. We simulated planets with surface temperatures of ~400 K, too hot to stabilize liquid water. Regardless of the surface conditions, however, the siderophile behavior of HPEs should produce longer-lived volcanism and magnetic activity in models, relative to models that assume lithophile behavior. No matter the regime of mantle dynamics, HPEs in the core are never sequestered into the crust, so they remain available to power convection in the deep interior over geologic time. For example, imposing plate tectonics versus stagnant-lid convection would change the predicted lifetimes of mantle melting and core convection, but implementing the siderophile behavior of HPEs should have the same directional effect (i.e., increasing those lifetimes). Our study thus implies that super-Earths are likely to remain geologically active for at least the main-sequence lifetimes of Sun-like stars.

Ultimately, our work shows that the distribution of HPEs within a planet is as important to planetary evolution as the bulk inventory of those elements. Their partitioning behavior is also as important in models as other factors that have received much attention, such as the viscosity of the lower mantle and the thermal conductivity of the core (discussed in Materials and Methods). Recent work emphasizes that exoplanet-hosting stars have concentrations of K, Th, and U that vary by factors of a few relative to those in Earth (52). We find that metal-silicate partitioning during core formation can change the abundances of HPEs in the mantle by at least that amount. Previous studies (16, 52) also predicted that planets with more internal heating are less likely to host dynamos. We conclude the opposite for super-Earths because we find that such heating is concentrated in the core, where it increases the core heat flux, rather than in the

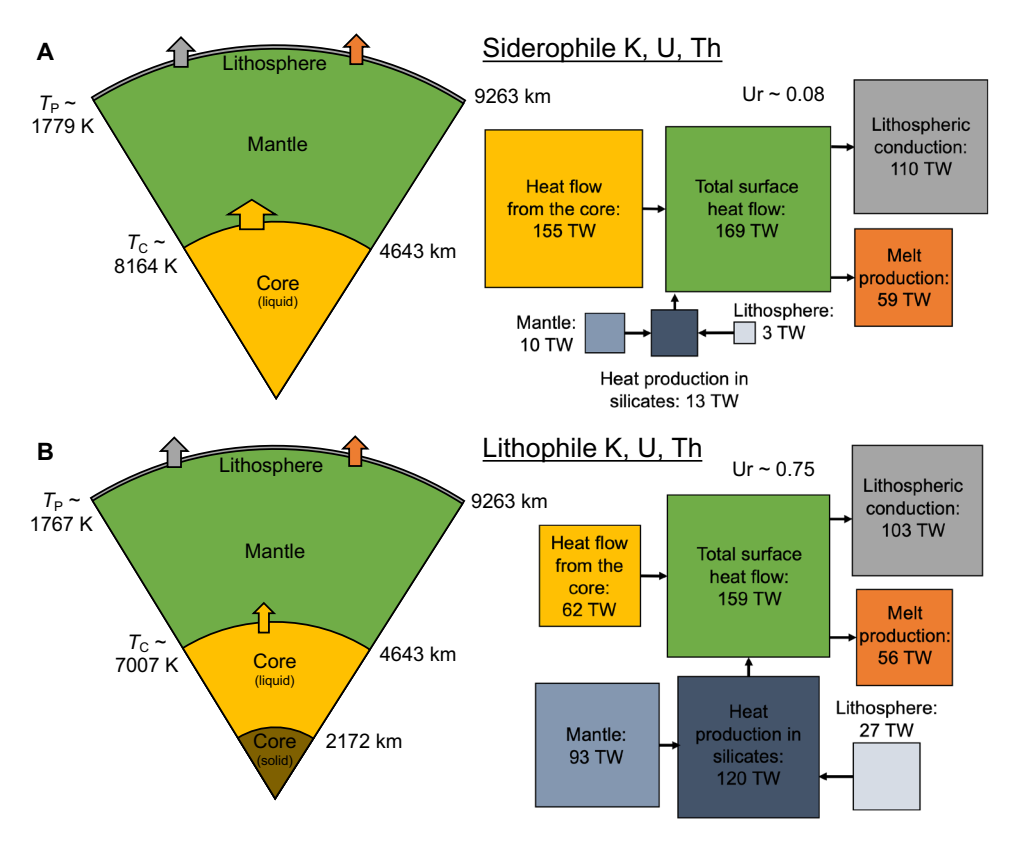


Fig. 2. Thermal evolution of super-Earths. Snapshots of the thermal evolution of super-Earths (4 M_F) after 4.5 billion years (Gyr). Cartoons on the left show the internal structure with the major layers to scale. Diagrams on the right show the global heat flow balance with the area of each square scaled to the amount of heat flux or production. HPEs are (A) partitioned between the mantle and core assuming metal-silicate equilibration at 500 GPa and 9000 K or (B) assumed to remain only in the silicates. Both models start with the same initial thermal state and use the lower-bound formula for the viscosity of post-perovskite (Materials and Methods).

mantle, which would decrease the core heat flux. Although our models here are only parameterized and neglect several processes (discussed in Materials and Methods), they clearly show that the siderophile behavior of HPEs transforms the heat budgets of super-Earths. Future models of individual worlds should consider the core as the furnace of planetary evolution.

MATERIALS AND METHODS

Chemical potentials

We first used the method described in the study on water partitioning (53) to calculate the chemical potentials of K2O, ThO2, and UO in metal (Fe and Fe_{5.4}O)/silicate (MgSiO₃) melt. The Gibbs free energy of a system under defined pressure (P), temperature (T), and solute concentration (x) can be expressed as

$$G(p, T, x) = \overline{G}(p, T, x) - TS_{\text{mix}}^{\text{system}}$$
(1)

where $\overline{G}(p, T, x)$ is the excess free energy and $S_{\text{miv}}^{\text{system}}$ is the ideal gas mixing entropy. Then, the chemical potential of K₂O/ThO₂/UO can be written as

$$\mu_{\rm K_2O/ThO_2/UO}(p,T,x) = \overline{\mu}_{\rm K_2O/ThO_2/UO}(p,T,x) - TS_{\rm mix}^{\rm K_2O/ThO_2/UO}(2)$$

Here, $\overline{\mu}_{K_2O/ThO_2/UO}(p,T,x)$ and $S_{mix}^{K_2O/ThO_2/UO}$ can be determined using

$$\overline{\mu}_{K_2O/ThO_2/UO}(p, T, x) = \overline{G}(p, T, x) + (1 - x) \frac{\partial \overline{G}(p, T, x)}{\partial x}$$
 (3)

$$S_{\text{mix}}^{\text{K}_2\text{O/ThO}_2/\text{UO}} = S_{\text{mix}}^{\text{system}} + (1 - x) \frac{\partial S_{\text{mix}}^{\text{system}}}{\partial x}$$
 (4)

The variations of $\overline{G}(p, T, x)$ per formula with respect to x (figs. S1 and S2) for our seven systems— $Fe_{1-x}(K_2O)_x$, $(Fe_{5,4}O)_{1-x}(K_2O)_x$, $(MgSiO_3)_{1-x}(K_2O)_x$, $(Fe_{5,4}O)_{1-x}(ThO_2)_x$, $(MgSiO_3)_{1-x}(ThO_2)_x$, $(Fe_{5.4}O)_{1-x}(UO)_x$, and $(MgSiO_3)_{1-x}(UO)_x$ —all exhibited a good fit when modeled with a linear equation

$$\overline{G}(p, T, x) = a + bx \tag{5}$$

where a and b are the fitting parameters. Consequently, $\overline{\mu}_{K,O/ThO_2/UO}$ (p,T,x) can be determined as a+b, and the uncertainties of $\overline{\mu}_{K,O/ThO_2/UO}(p,T,x)$ can be obtained through SE propagation considering the uncertainties of a and b determined from the lin-

ear fitting.

The $S_{\text{mix}}^{K_2\text{O/ThO}_2/\text{UO}}$ for the seven systems, computed using Eq. 4, are as follows $S_{\text{mix}}^{K_2\text{O/ThO}_2/\text{UO}} = \frac{1}{2} \left(2 \ln \frac{2x}{x} + \ln \frac{x}{x} \right)$ (6)

$$S_{\text{mix}}^{K_2 \text{O in Fe}} = -k_B \left(2\ln \frac{2x}{1+2x} + \ln \frac{x}{1+2x} \right)$$
 (6)

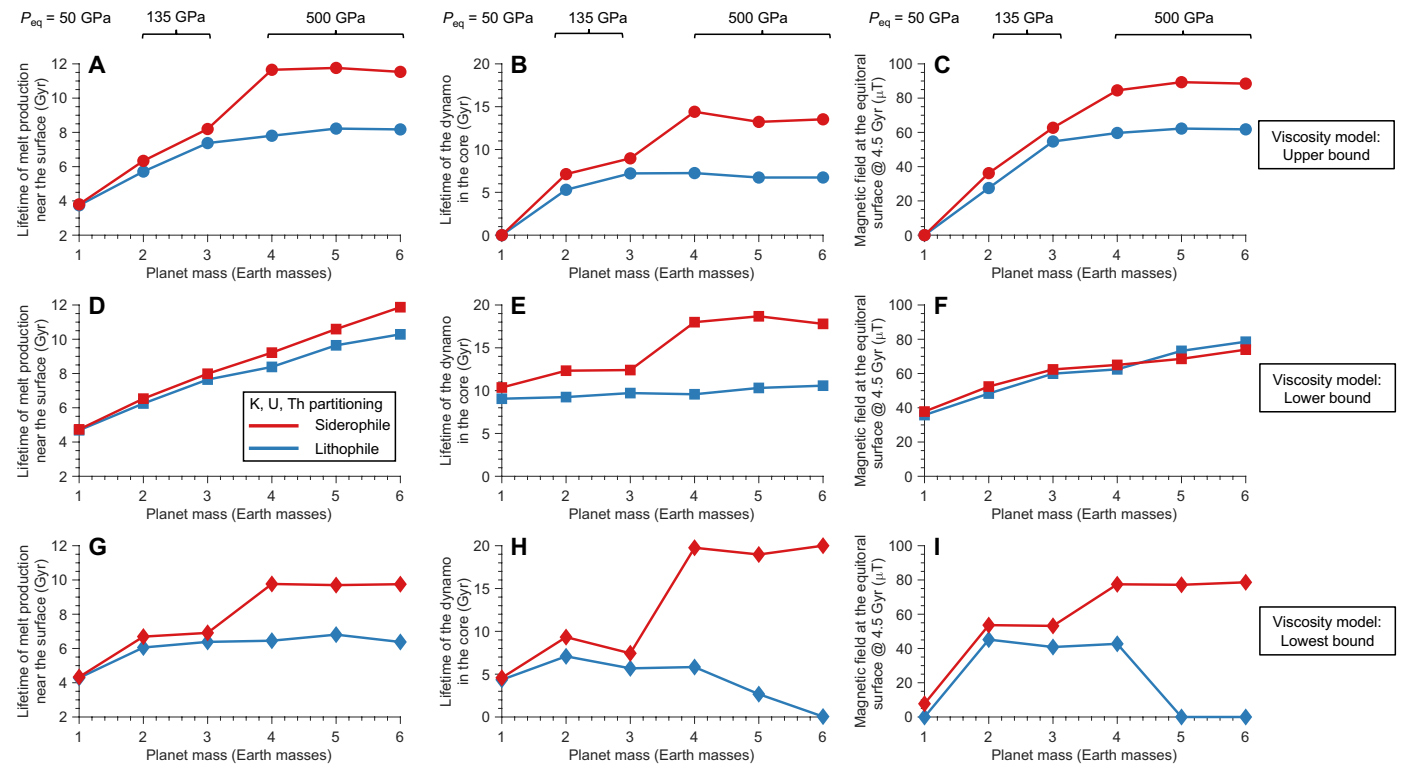


Fig. 3. Volcanism and dynamos in super-Earths. Lifetimes of volcanism and dynamos in super-Earths in our models, which changed on the basis of the siderophile versus lithophile behavior of HPEs. We simulated the thermal evolution of terrestrial planets, with total masses of 1 to 6 $M_{\rm E}$, in the stagnant-lid regime for 20 Gyr (see Materials and Methods). In each subplot, red symbols represent models that assumed siderophile behavior for HPEs, using the equilibrium pressures listed at the top of the figure. Blue symbols represent models where the HPEs remained lithophile. Lines are drawn between symbols for illustration purposes only. From top to bottom, each row shows the output from models that used the (**A** to **C**) upper, (**D** to **F**) lower, and (**G** to **I**) lowest bound for the rheology of the lower mantle (see Materials and Methods), respectively. From left to right, each column shows [(A), (D), and (G)] when melt production near the surface ceased forever, [(B), (E), and (H)] when fluid motion in the core stopped, and [(C), (F), and (I)] the strength of the dipolar component at the surface after 4.5 Gyr.

$$S_{\text{mix}}^{K_2 \text{O in Fe}_{5,4} \text{O}} = -k_B \left(2\ln \frac{2x}{6.4 - 3.4x} + \ln \frac{1}{6.4 - 3.4x} \right)$$
 (7)

$$S_{\text{mix}}^{K_2\text{O in MgSiO}_3} = -k_{\text{B}} \left(2\ln \frac{2x}{5 - 2x} + \ln \frac{3 - 2x}{5 - 2x} \right)$$
 (8)

$$S_{\text{mix}}^{\text{ThO}_2 \text{ in Fe}_{5.4}\text{O}} = -k_{\text{B}} \left(\ln \frac{x}{6.4 - 3.4x} + 2\ln \frac{1 + x}{6.4 - 3.4x} \right)$$
(9)

$$S_{\text{mix}}^{\text{ThO}_2 \text{ in MgSiO}_3} = -k_B \left(\ln \frac{x}{5 - 2x} + 2 \ln \frac{3 - x}{5 - 2x} \right)$$
 (10)

$$S_{\text{mix}}^{\text{UO in Fe}_{5,4}\text{O}} = -k_{\text{B}} \left(\ln \frac{x}{6.4 - 4.4x} + \ln \frac{1}{6.4 - 4.4x} \right)$$
 (11)

$$S_{\text{mix}}^{\text{UO in MgSiO}_3} = -k_{\text{B}} \left(\ln \frac{x}{5 - 3x} + \ln \frac{3 - 2x}{5 - 3x} \right)$$
 (12)

Then, at equilibrium when $\mu_{\text{K}_2\text{O/ThO}_2/\text{UO}}^{\text{Fe}_{\text{s}_4}\text{O}}(p, T, x) = \mu_{\text{K}_2\text{O/ThO}_2/\text{UO}}^{\text{MgSiO}_3}(p, T, y)$,

the partition coefficients that we need, $D_{\rm K_2O/ThQ_2/UO}^{\rm Fe_{5,4}O-MgSiO_3} = x/y$, can be readily obtained using Eq. 2, and the associated errors are propagated from the uncertainties of the chemical potentials. We calculated the chemical potentials of ThO and UO₂ by adopting alchemical free energy method. For instance, the Th atom in the ThO₂-bearing metal or silicate melt was converted to U atom to obtain the chemical potentials of UO₂. More details of this method can be found in previous publications (54, 55).

Molecular dynamics simulations

We conducted simulations of the iron melt using 64 Fe atoms, the iron-alloy melt using 54 Fe and 10 O atoms, and the silicate melt using 32 formula units of MgSiO $_3$. Subsequently, K $_2$ O, ThO $_2$, and UO were introduced into the supercells. Born-Oppenheimer AIMD simulations were performed using the projector augmented wave method (56, 57) and PBEsol exchange-correlation functional (58), as implemented in Vienna Ab initio Simulation Package (59). Valence configurations for elements were specified as follows: Fe $3p^63d^74s^1$, Mg $2p^63s^2$, Si $3s^23p^2$, O $2s^22p^4$, K $3s^23p^64s^1$, Th $6s^26p^66d^27s^2$, and U $6s^26p^65f^36d^17s^2$. Previous studies (60–65) tested these PAW potentials by comparing with all-electron calculations and found good agreement up to the terapascal level. Thermal equilibrium between

ions and electrons was maintained using the Mermin functional (66). We tested the relativistic effect for heavy elements Th and U by doing spin orbit coupling calculations and found that the relativistic effect behaves similarly in metal and silicate phases, resulting in no significant change in the calculated partition coefficients. We evaluated the magnetic states of Th and U in silicate melt and Fe, Th, and U in metal melt using spin-polarized calculations. We found that all atoms remain in a nonmagnetic state when the pressure exceeds 135 GPa. Only U in silicate melt and Fe in metal melt exhibit a small magnetic moment (<0.75 μB) at 50 GPa. Previous studies indicate that ignoring magnetism does not significantly affect metal-silicate partitioning of elements such as H (53), noble gas (67), and Pu (actinide element like Th and U) (68). The agreement between our calculated partition coefficients and experimental data at 50 GPa supports this approximation, especially considering our main focus is on super-Earth scenarios. Thus, all our simulations were performed without spin polarization. Each simulation was run for up to 20,000 steps with a timestep of 1.0 fs. Brillouin zone sampling was done at the gamma point only, with a plane-wave energy cutoff set to 600 and 800 eV for liquid iron/iron-alloy and silicate melts, respectively. For Th/U-bearing silicate melts, a plane-wave energy cutoff of 680 eV was used. To correct for pressure in iron/iron-alloy, a $2 \times 2 \times 2$ Monkhorst-Pack mesh of *k*-points was used because of the relatively small system size. The effect of the k-point mesh on the calculated chemical potentials is negligible (table S6). We corrected the difference in the energy cutoff between silicate melts and Th/U-bearing silicate melts with thermodynamic perturbation using the secondorder cumulant expansion. We used a NVT canonical ensemble (i.e., number of atoms, volume, and temperature remain constant during simulation) with temperature regulation achieved through a Nosé-Hoover thermostat (69). Equilibrium volume was determined by conducting several NVT simulations at different volumes around the target pressure and fitting the resulting pressure-volume data. Radial distribution function and mean square displacement analyses were conducted to ensure the liquid state of our simulated systems.

Thermodynamic integration

We computed the Gibbs free energy of iron/iron-alloy and silicate melts through thermodynamic integration from the ideal gas state (70). This involved integrating the difference in internal energy between the melt (U_1) and the ideal gas (U_0) with respect to the coupling parameter λ , as follows

$$\Delta G_{0-1} = \int_0^1 d\lambda \langle U_1(R) - U_0(R) \rangle_{\lambda} \tag{13}$$

To address the numerical instabilities arising from the proximity of noninteracting atoms at $\lambda = 0$, we used the variable transformation approach (70) with $\lambda(x) = \left(\frac{x+1}{2}\right)^{1/(1-k)}$, leading to

$$\Delta G = \frac{1}{2(1-\kappa)} \int_{-1}^{1} f[\lambda(x)] \lambda(x)^{k} dx$$
 (14)

where we chose k=0.8. An eight-point Gauss-Lobatto rule was used to compute this integral. The errors in internal energies were determined using the blocking average method (71). The errors of the numerically integrated free energies were derived through SE propagation, i.e., for a numerical integral $I = \sum_i \omega_i f_i$, $\sigma^2(I) = \sum_i \omega_i^2 \sigma^2(f_i)$, where $\sigma(A)$ represents the error for the quantity A. We also tested using

Weeks-Chandler-Andersen fluid rather than the simple ideal gas as the reference state of liquid and found the difference in free energies is negligible. More sophisticated integrated pathways are unlikely to change significantly our partitioning results as they only result in difference in free energy at tens of milli–electron volts per atom (72), which is around one order of magnitude smaller than the error bar of chemical potential (table S2).

The Gibbs free energy of the ideal gas was computed as

$$G^{ig} = F^{ig} + PV = -k_{\rm B}T \sum_{i} \ln\left(\frac{V^{N_i}}{N_i! \Lambda_i^{3N_i}}\right) + PV$$
 (15)

Here, $k_{\rm B}$ represents the Boltzmann constant, T denotes temperature, P stands for pressure, V represents volume, N_i signifies the number of atoms for element i, Λ_i denotes the thermal wavelength of element i given by $\Lambda_i = h/(2\pi M_i k_{\rm B} T)^{1/2}$, with h representing the Plank's constant and M_i representing the atomic mass of element i. All calculations were calibrated to the target pressures adopting the thermodynamic relation

$$G(P_2, T) - G(P_1, T) = \left(\int_{P_1}^{P_2} V dP\right)_T$$
 (16)

Thermal evolution models

We used parameterized models for the thermal evolution of terrestrial exoplanets. These models assume that the silicate mantle is fully solid, while the metallic core is fully molten. In the immediate aftermath of planetary accretion, the silicate mantle should be at least partially molten. Prior studies show that a magma ocean in the mantle could solidify from the bottom upward in ~10 to 100 million years (Myr) (73). Here, our models start after this solidification is complete, however long it takes. In other words, t in our models is the time after the mantle has fully solidified, which is less than the time after the planet has accreted. We chose not to model planetary accretion in detail because our focus is on the long-term evolution of terrestrial planets.

Our models also do not yet include a basal magma ocean (BMO). As discussed below, a large reservoir of molten silicates could survive in the lower mantle if the mantle crystallizes from the middle outward. This BMO could take billions of years to solidify, because the overlying, solid mantle is insulating and the adjacent core is a heat sink (74). Adding a BMO to our models is a priority but will introduce additional complexity. We chose to start with models that assume a fully solid mantle to set a foundation for future models that include a BMO.

In our models, we first specify the radial structure and thermophysical properties of each planet. We follow (45) in assuming that the core constitutes 32.5% of the total planetary mass, as for Earth. To isolate the effects of individual parameters in our models, we need to assume that every planet operates with the same mode of mantle convection. We chose to model stagnant-lid convection, which is perhaps the most natural (albeit not the most Earth-like) mode for terrestrial planets. For simplicity, we adapted the scaling laws for stagnant-lid convection from (8) and the references therein, unless otherwise cited. However, we augmented their approach to include the heat flux from the core in the mantle's heat budget and to track the evolution of the core in detail to better predict when a dynamo would exist. We also changed the treatment of mantle viscosity to use the results of (50) and (51). Last, we simplified the description of

melt production to enable more straightforward comparisons between models.

In this section, we first describe the governing equations for our model. Next, we explain how we run an individual model. Then, we present all the models that we ran for this study. Last, we discuss some limitations of our models and priorities for future work.

Governing equations

Figure S10 is a cartoon of the internal structure, labeling the properties that we track over time. The temperature of the mantle changes with time (t) according to its energy budget

$$V_{\rm M}\rho_{\rm M}C_{\rm M}\frac{dT_{\rm M}}{dt} = H_{\rm M} + Q_{\rm C} - Q_{\rm M}$$

$$\tag{17}$$

where $V_{\rm M}$, $\rho_{\rm M}$, and $C_{\rm M}=1250~{\rm J~kg^{-1}~K^{-1}}$ are the volume, average density, and specific heat capacity of the mantle, respectively. Here, $T_{\rm M}$ is the potential temperature of the mantle (i.e., the projection of the adiabatic thermal gradient in the convective mantle to the planet's surface). The total amount of radiogenic heating in the convective mantle is $H_{\rm M}$, which does not include any contribution from HPEs in the lithosphere. The total heat flux from the core into the mantle is $Q_{\rm C}$. We assume that the total mantle heat flux $(Q_{\rm M})$ is split into two parts: heat conducted into the stagnant lid $(Q_{\rm M,cond})$ and heat associated with the production and transport of melt $(Q_{\rm M,melt})$.

The viscosity of the solid silicates governs the rate at which the mantle and core can lose heat. We assume that the mantle viscosity changes with temperature and pressure as

$$\eta(T, P) = \eta_0 \exp\left(\frac{H}{RT} - \frac{E}{RT_0}\right)$$
 (18)

where η_0 is a reference viscosity at a reference temperature ($T_0 = 1600 \text{ K}$) and R is the universal gas constant (50). Here, E is an activation energy. The effective enthalpy, H = E + PV, depends on the effective activation volume, $V = V_0 \exp(-P/P_{\text{decay}})$. To calculate the viscosity of the upper mantle, we take $E = 300 \text{ kJ mol}^{-1}$, P = 0, and $\eta_0 = 10^{20} \text{ Pa·s}$ (50). For the lower mantle, we test three sets of values that reflect the current uncertainty on the rheology of post-perovskite (50). We use the "lower bound" and "upper bound" from table 2 of (50). The lower bound has $E = 162 \text{ kJ mol}^{-1}$, $V_0 = 1.4 \times 10^{-6} \text{ m}^3 \text{ mol}^{-1}$, $P_{\text{decay}} = 1610 \text{ GPa}$, and $\eta_0 = 1.9 \times 10^{21} \text{ Pa·s}$, while the upper bound features $E = 780 \text{ kJ mol}^{-1}$, $V_0 = 1.7 \times 10^{-6} \text{ m}^3 \text{ mol}^{-1}$, $P_{\text{decay}} = 1100 \text{ GPa}$, and $\eta_0 = 1.05 \times 10^{34}$ Pa·s. As expressed by their names, the lowerbound rheology always predicts a less viscous lower mantle than the upper-bound rheology. However, the upper-bound rheology implies that the lower mantle viscosity is relatively insensitive to planetary mass; the effects of increasing pressure and temperature in larger planets balance each other out. In contrast, the lower-bound rheology predicts that massive planets have more viscous lower mantles (e.g., by ~6 orders of magnitude for ~6- M_E versus ~1- M_E planets). Last, Karato (51) argued that lower mantle viscosity could decrease with increasing planetary mass, perhaps by ~2 orders of magnitude up to \sim 6 $M_{\rm E}$. To produce this behavior, our "lowestbound" viscosity model uses $E = 650 \text{ kJ mol}^{-1}$, $V = 0.2 \times 10^{-6} \text{ m}^3 \text{ mol}^{-1}$ (i.e., infinite P_{decay}), and $\eta_0 = 10^{33}$ Pa·s. Figure S11 shows the lower mantle viscosity predicted by all three models, when $T_{\rm M} = 1600$ K, as a function of pressure at the CMB.

Convective vigor in the mantle increases with its temperature. At each timestep in our models, we first calculate the Frank-Kamenetskii parameter

$$\Theta_{\rm FK} = \frac{E(T_{\rm M} - T_{\rm S})}{RT_{\rm M}^2} \tag{19}$$

where we set the surface temperature to $T_{\rm S}$ = 400 K always. Varying $T_{\rm S}$ by up to a few hundred kelvins would obviously imply hugely different surface conditions but would not substantially change the thermal evolution of the mantle and the core, if we continued to assume that the mantle operated in the stagnant-lid regime. Therefore, we can illustrate the main effects of the siderophile behavior of HPEs using models with a fixed $T_{\rm S}$. Next, we compute the Rayleigh number of the mantle

$$Ra = \frac{\rho_{\rm M} g \alpha_{\rm M} (T_{\rm M} - T_{\rm S}) (R_{\rm P} - R_{\rm C})^3}{\kappa_{\rm M} \eta}$$
 (20)

where g is the gravitational acceleration at the surface; $\alpha_{\rm M} = 10^{-6}~{\rm K}^{-1}$ and $\kappa_{\rm M} = 10^{-6}~{\rm m}^2~{\rm s}^{-1}$ are the thermal expansivity and thermal diffusivity of the mantle, respectively; and $R_{\rm P}$ and $R_{\rm C}$ are the radii of the planet and core (table S7), respectively. We then compute a characteristic velocity for convection as in (8), based on "scaling I" for linear viscosity with a stress exponent of n=1 from (75)

$$v = \frac{0.05\kappa_{\rm M}}{R_{\rm P} - R_{\rm C}} \left(\frac{\rm Ra}{\Theta_{\rm FK}}\right)^{\frac{2}{3}} \tag{21}$$

In the stagnant-lid regime, the temperature contrast across the convective boundary layer depends on the temperature dependence of viscosity (75–79)

$$\Delta T_{rh} \approx a_{rh} \Theta_{FK}^{-1} (T_{M} - T_{S}) = \frac{a_{rh} R T_{M}^{2}}{E}$$
 (22)

where α_{rh} is a constant. The mantle heat flux per unit area is then

$$F_{\rm M} \approx 0.5 k_{\rm M} \Theta_{\rm FK}^{-\frac{4}{3}} {\rm Ra}^{\frac{1}{3}} \left(\frac{T_{\rm M} - T_{\rm S}}{R_{\rm P} - R_{\rm C}} \right)$$
 (23)

where positive values indicate that heat is moving out of the mantle (75). Here, $k_{\rm M} \sim 5$ W/(m·K) is the thermal conductivity of the upper mantle (8). Last, the mantle heat flux that is conducted into the stagnant lid is simply that flux multiplied by the surface area of the mantle: $Q_{\rm M,cond} = (4/3)p(R_{\rm P} - \delta_u)^2 F_{\rm M}$, where δ_u is the thickness of the lithosphere.

We then use an energy balance to determine how the thickness of the lithosphere changes over time. The lid changes in response to the mantle heat flux (8, 80, 81)

$$\rho_{\rm M}C_{\rm M}\left(T_{\rm M}-T_{\rm B}\right)\frac{d\delta_u}{dt} = -F_{\rm M}-k_{\rm M}\left.\frac{\partial T}{\partial z}\right|_{z=R_{\rm D}-\delta_u} \tag{24}$$

The rightmost term is a boundary condition that depends on the amount and distribution of radiogenic heating in the lithosphere. Unterborn *et al.* (8) tracked the thicknesses of the crust and lithosphere separately, because the crust (a compositional layer) can be thinner than the lithosphere (a layer defined on the basis of its mechanical and thermal properties). In their models, HPEs are concentrated within the crust, whereas any lithosphere below the crust has the same concentration of HPEs as the rest of the mantle. Mantle convection tends to entrain and recycle any crust that becomes thicker than the lithosphere. For simplicity, we assume here that the HPEs are distributed uniformly throughout the lithosphere. We do not separately track the thickness of the crust or its inventory of

HPEs. Because our study is not focused on the detailed structure of the crust and lithosphere, this simplification does not affect our main results. In any case, the temperature at the base of the lithosphere is

$$T_{\rm B} = T_{\rm M} - \Delta T_{rh} = T_{\rm M} \left(1 - \frac{a_{rh}RT_{\rm M}}{E} \right) \tag{25}$$

where the rightmost term relates to how hot the silicates need to become to participate in mantle convection (75). We set $\alpha_{rh} \sim 2.5$ following (8), although Solomatov and Moresi (75) suggested that $\alpha_{rh} \sim 2.4$ for the viscosity scaling used in Eq. 21. This discrepancy does not affect our results. Last, the boundary condition used in Eq. 24 is

$$k_{\rm M} \left. \frac{\partial T}{\partial z} \right|_{z=R_{\rm D} - \delta_{\rm u}} = 0.5 x_{\rm u} \delta_{\rm u} - \frac{k_{\rm M} \left(T_{\rm B} - T_{\rm S} \right)}{\delta_{\rm u}} \tag{26}$$

where x_u is the volumetric rate of radiogenic heat production (i.e., in units of watts per cubic meter) in the lithosphere, i.e., the sum of individual contributions from K, Th, and U (8). This equation represents the steady-state thermal gradient within the lithosphere, where conductive heat transport balances radiogenic heating (82). As explained below, the lithosphere and mantle have different rates of radiogenic heat production.

Melt production removes heat from the mantle and sequesters HPEs in the lithosphere. We assume that melting begins below the lithosphere at a pressure that increases with $T_{\rm M}$

$$P_i = 1 \text{ GPa} \left(\frac{T_{\text{M}} - 1423 \text{ K}}{100 \text{ K}} \right) \tag{27}$$

based on a solidus for dry peridotite (82–84). The equivalent depth is $d_{\text{melt}} = P_i/(\rho_{\text{L}}g)$, where $\rho_{\text{L}} \sim 3300 \text{ kg m}^{-3}$ is the average density of the lithosphere. Melting stops at the base of the lithosphere, at a final pressure of

$$P_f = \rho_L g \delta_u \tag{28}$$

The melt fraction depends on the difference between these two pressures

$$\phi = 0.075 \left(\frac{P_i - P_f}{1 \text{ GPa}} \right) \tag{29}$$

Following (8) and the references therein, the volumetric rate of melt production is

$$f_{\rm m} = 17.8\pi R_{\rm P} \nu \left(d_{\rm melt} - \delta_{\nu} \right) \Phi \tag{30}$$

In this study, we do not estimate or compute the relative fraction of extrusive volcanism versus intrusive magmatism, simply the total rate of near-surface melting. The heat flux associated with melt production is then

$$Q_{\rm M,melt} = f_{\rm m} \rho_{\rm M} \left(C_{\rm M} \Delta T_{\rm m} + L_{\rm M} \right) \tag{31}$$

where $\Delta T_{\rm m} = T_{\rm M} - (6.6766 \times 10^{-4} \, {\rm K m}^{-1}) d_{\rm melt} - T_{\rm S}$ is the difference between the temperature of the melt at the base of the lithosphere versus at the surface (8). The latent heat of melting for the silicates is $L_{\rm M} = 600 \, {\rm kJ \, kg}^{-1}$ (8). Last, HPEs are incompatible elements, so they partition into the lithosphere because of melt production. However, if the lithosphere thins (i.e., $d\delta_u/dt < 0$), then some HPEs are recycled back into the mantle. In each timestep, we track the change(s) in the lithospheric heat production for each isotope (8, 82)

$$\frac{dH_{L,i}}{dt} = \frac{x_{m,i}f_m}{\Phi} \left[1 - (1 - \Phi)^{\frac{1}{D_i}} \right]$$

$$- x_{u,i} \left(f_m - 4\pi \left[R_P - \delta_u \right]^2 \min \left[0, \frac{d\delta_u}{dt} \right] \right) - \lambda_i H_{L,i}$$
(32)

where $x_{m,i}$ is the volumetric rate of heat production from an individual isotope in the mantle and λ_i is the isotope-specific decay constant. The partition coefficients are $D_i = 0.0011$, 0.0012, and 0.0029 for K, U, and Th, respectively. What is added to the crust is subtracted from the mantle, and vice versa (8, 82)

$$\frac{dH_{\mathrm{M},i}}{dt} = -\frac{x_{\mathrm{m},i}f_{\mathrm{m}}}{\phi} \left[1 - (1 - \phi)^{\frac{1}{D_{i}}} \right] + x_{u,i} \left(f_{\mathrm{m}} - 4\pi \left[R_{\mathrm{P}} - \delta_{u} \right]^{2} \min \left[0, \frac{d\delta_{u}}{dt} \right] \right) - \lambda_{i} H_{\mathrm{M},i}$$
(33)

In general, sequestering HPEs in the crust leads to colder mantle temperatures over time and thus less melt production and a shorter lifetime of volcanism.

We use a boundary layer model to calculate the heat flux out of the core. That is, we assume that the steady-state thickness of the boundary layer results in a Rayleigh number close to the critical value of $\sim 10^3$ for convection (i.e., the entire boundary layer can be mobile, unlike in the stagnant-lid atop the mantle). The thickness of that boundary layer above the core is then

$$\delta_{\rm l} = \left[\frac{10^3 \kappa_{\rm l} \eta \left(0.5 \left[T_{\rm C} + T_{\rm L} \right] \right)}{\rho_{\rm l} g_{\rm l} \alpha_{\rm l} \left(T_{\rm C} - T_{\rm L} \right)} \right]^{\frac{1}{3}}$$
 (34)

where $T_{\rm L}$ and $T_{\rm C}$ are the temperatures of the basal mantle and the upper core, respectively (45). To calculate the temperature in the lower mantle, we assume that $T_{\rm L} = T_{\rm P}[\rho_{\rm I}/(4100~{\rm kg/m^3})]^G$, where G ranges from ~1.11 to 1.01 (table S7). This expression reproduces the adiabat from figure 2 of (50). In the lower mantle, $k_{\rm L}$, $\rho_{\rm L}$, $g_{\rm L}$, and $\alpha_{\rm L}$ are the local thermal diffusivity, density, gravitational acceleration, and thermal expansivity, respectively, all calculated as in (45). The total heat flow across the CMB is then

$$Q_{\rm C} = 4\pi R_{\rm C}^2 k_{\rm l} \left(\frac{T_{\rm C} - T_{\rm L}}{\delta_{\rm l}}\right) \tag{35}$$

Our approach assumes whole-mantle convection. In larger super-Earths, adiabatic compression may cause layered convection (47, 48). Because our models do not include layered mantle convection, we studied only super-Earths up to a mass of 6 $M_{\rm E}$. However, larger super-Earths are rare in our galaxy. Observations have revealed that exoplanets larger than ~1.6 Earth radii (~4 to 5 $M_{\rm E}$) typically have thick volatile envelopes, meaning that they are not rocky (72). Statistics aside, missions such as the NASA Transiting Exoplanet Survey Satellite and follow-up observations will provide mass and radius measurements that can guide future models.

We model the core's response to cooling exactly as in (45), which was heavily based on (85). The heat budget for the core is

$$Q_{\rm C} = Q_{\rm RC} + Q_{\rm SC} + Q_{\rm PC} + Q_{\rm GC} + Q_{\rm LC} + Q_{\rm IC}$$
 (36)

where the total heat flow is partitioned into six heat flow terms on the right side: radiogenic heat (RC), secular cooling (SC), precipitation of light elements near the core/mantle boundary (PC), gravitational energy associated with the exclusion of light elements from the inner core (GC), the latent heat of freezing for the inner core (LC), and heat conducted out of the inner core (IC), assuming that the inner core has effectively infinite thermal conductivity (45). We can write each of the terms, except $Q_{\rm RC}$, in the form $Q_i = \Theta_i(dT_{\rm C}/dt)$, where Θ_i is a function only of the thermophysical parameters of the core (45). Thus, we calculate the cooling rate of the core (45)

$$\frac{dT_{\rm C}}{dt} = \frac{Q_{\rm C} - Q_{\rm R}}{\Theta_{\rm SC} + \Theta_{\rm PC} + \Theta_{\rm GC} + \Theta_{\rm LC} + \Theta_{\rm IC}}$$
(37)

We use a fourth-order polynomial to parameterize the density profile of the core. Therefore, the equations for the individual heat flow terms are algebraically complex. Interested readers are encouraged to consult (45), for the complete details, including the definition of the liquidus in the core. Here, we calculate the thermal conductivity of the core as $k_c = -35.64 \text{ W m}^{-1} \text{ K}^{-1} + (0.027 \text{ W m}^{-1})$ K^{-2}) T_D , where T_D is the average temperature in the liquid portion of the core. This fitted linear temperature dependence of the thermal conductivity is based on the computed results (86) corrected by electron-electron scattering (87) for the Fe_{0.79}Si_{0.08}O_{0.13} liquid using an adiabat of $T_{\rm ICB}$ = 5500 K. We assume that the super-Earths have Earth-like abundances of light elements, meaning that the solidification of the inner core releases gravitational energy. After the inner core nucleates, its growth rate (dR_I/dt) is directly proportional to the core's cooling rate (dT_C/dt) . Our models self-consistently capture how the flux of light elements from the inner core depresses the liquidus of the outer core.

We use the dissipation budget for the core to determine when a dynamo may exist (45, 85). When positive dissipation ($\Phi > 0$) is available, we use mixing length theory and the Coriolis-Inertial-Archimedes (CIA) and the magneto-Archimedes-Coriolis (MAC) force balances to estimate the strength of the dipole component of the magnetic field (88). Note that we do not use the same velocity scalings for the liquid core and the solid mantle because their viscosities are so different. For example, from mixing length theory, the strength of the magnetic field in the core is (89)

$$B_{\rm C} = \left[2c\mu_0 \left(\rho_0 R_{\rm C}^2 \Phi^2 \right)^{\frac{1}{3}} \right]^{\frac{1}{2}}$$
 (38)

where $c \sim 0.63$ is a constant of proportionality, ρ_0 is the density at the center of the core, and μ_0 is the permeability of free space. The surface field strength of the dipole component is then

$$B_{\rm S} = \frac{1}{7} B_{\rm C} \left(\frac{R_{\rm C}}{R_{\rm p}}\right)^3 \tag{39}$$

where the prefactor of $^{1}/_{7}$ represents an Earth-like power spectrum for the magnetic field (89). We report the magnetic field strength using the results from mixing length theory because they are closest to the strength of Earth's magnetic field for a 1- $M_{\rm E}$ planet (i.e., within a factor of a few). Using the MAC or CIA scaling laws would return lower field strengths for all planets, but with the same effects from changing planetary mass and/or the partitioning behavior of HPEs.

In the core, there are two competing effects of radiogenic heating on the prospects for a dynamo. For a fixed amount of heat flow extracted into the mantle, more radiogenic heating in the core tends to decrease the dissipation available for a dynamo, because radiogenic heating is less efficient as a power source than secular cooling and the exclusion of light elements from the growing inner core (if existing) (85). However, we should not assume that the core heat flux stays fixed if the partitioning behavior of HPEs changes. Radiogenic heating also slows the cooling of the core. Partitioning radioactive elements into the core means that they are less abundant in the mantle, implying that the heat flow across the CMB should be relatively higher, which would increase the available dissipation. Our models revealed that this second effect is more important, meaning that adding HPEs to the cores of super-Earths bolsters the chance that they would host a strong, long-lived dynamo.

The Urey ratio is a fundamental parameter used to characterize the heat budget of the mantle. Following (49), we can define the conventional Urey ratio as $\text{Ur} = (H_{\text{L}} + H_{\text{M}})/Q_{\text{M}}$ and the convective Urey ratio as $\text{Ur}_{\text{conv}} = H_{\text{M}}/Q_{\text{M}}$. With either definition, Urey ratios near or above ~0.5 to 1 would imply that internal heating powers mantle convection, as typically assumed for super-Earths (8, 50, 90). We found that the siderophile behavior of HPEs may instead lead to small Urey ratios for larger terrestrial planets, meaning that internal heating hardly contributes to the mantle's heat budget. Rather, our models predict that heating from below and cooling from above drives mantle convection in super-Earths.

Initial conditions

Table S7 lists temperatures that are probably relevant to the evolution of planetary cores. Here, we assume that the silicate mantles and metallic cores have Earth-like abundances of iron and other major elements. Following previous studies, we use a fiducial "light element" to parameterize the composition of the core (45, 85). Light elements lower the melting temperature of the core relative to that of a pure iron/nickel alloy. As the core cools, we assume that an inner core freezes outward from the center of the core. Blaske and O'Rourke (45) reported the temperature at the CMB when the inner core first nucleates ($T_C[R_I=0]$). Noack and Lasbleis (44) calculated three other temperatures that are important to the core. First, the lowest temperature expected at the CMB is $T_{C,cold}$, the adiabatic temperature at the bottom of the mantle, assuming that the mantle is ~2000 K at a depth of ~200 km. We use the same qualitative definition of $T_{C,cold}$ in this study. However, we calculate the mantle adiabat using the procedure described above, because Noack and Lasbleis (44) used an approach that is valid only up to planetary masses of \sim 2 $M_{\rm E}$. Second, the hottest temperature that we assume for the top of the core is $T_{C,hot}$, the liquidus temperature at the base of the mantle. We calculated this temperature from (37), assuming an Earth-like mantle composition. Last, an intermediate expected temperature is $T_{C,warm}$, the solidus temperature of the basal mantle (fig. S11B). We also calculated this temperature following (37). We found that a core that is vigorously convective with a CMB temperature of $T_{C,hot}$ or $T_{C,warm}$ should be fully liquid. Because $T_{C,hot} > T_{C,warm} > T_{C,cold}$, our assumption that the mantle remains fully solid is self-consistent as long as the core starts no hotter than $T_{C,warm}$ and cools over time, which is how our models behave.

We started each model with the same thermal state to isolate and identify the effects of planetary mass and the partitioning behavior of the HPEs. The pressure and temperature conditions corresponding to core formation may vary depending on planet accretion processes (e.g., the number, timing, and energy of giant impacts). Nevertheless, at high pressures (>300 to 400 GPa) U and Th become strongly siderophile, and the partition coefficient of K only varies within a small range (Fig. 1). Thus, using partition coefficients of the HPEs obtained at somewhat different pressure and temperature conditions relevant to core formation for these large exoplanets does

not influence our overall conclusions. Here, t=0 represents the time at which the mantle has fully solidified, after it was at least partially molten in the aftermath of planetary accretion. At that time, we set the potential temperature of the mantle to $T_{\rm M}=2000$ K. We assume that the lithosphere has an initial thickness of $d_u=100$ km but contains no HPEs to start. We set $T_{\rm C}=T_{\rm C,warm}$ although hotter temperatures are also plausible, which would lead to stronger and longer-lived dynamos and melt production. We used Euler's method to solve the governing equations with a timestep of $\Delta t=0.5$ thousand years until t=20 Gyr, at which time melt production and the dynamo had ceased in all models. We verified that using a smaller timestep would not change the model output.

Sensitivity tests

To present the results presented in Fig. 3, we ran 72 models. We explored all combinations of four planetary masses, two partitioning behaviors for HPEs (i.e., siderophile versus lithophile), three viscosity models for post-perovskite in the lower mantle, and three values of the thermal conductivity of the core (i.e., 75, 100, and 125% of the nominal value determined as described above). Figures S12 to S17 show the detailed output from the models for a 4-M_E super-Earth using the nominal thermal conductivity for the core. The last nonzero values in subpanels (F) and (I) were extracted for Fig. 3. All the models display similar trends. The planets start hot and cool monotonically over time. The heat fluxes out of the mantle and core are relatively huge at initially but gradually decrease as the mantle becomes increasingly viscous. The lithosphere quickly adjusts from its initial thickness to an equilibrium value and then steadily thickens as the mantle cools. Melt production slows over time because the initial and final depths of melting gradually converge. Last, the predicted magnetic field strength mostly declines over billions of years. Our models predict a spike in field strength lasting <1 Gyr when the inner core nucleates. However, more detailed studies of Earth's dynamo indicate that the nucleation of the inner core might not produce an observable change in the surface field intensity (91, 92), which agrees with the lack of scientific consensus about whether any such spike exists in Earth's paleomagnetic record. The partitioning behavior of HPEs does not affect these trends. However, moving HPEs to the core keeps internal temperatures hot and heat fluxes high in these models, leading to longer predicted lifetimes of nearsurface melt production and magnetic fields.

Figures S18 and S19 show the summary statistics from the models with higher- and lower-than-nominal thermal conductivity in the core, respectively. Relative to Fig. 3, these plots show clear trends. The thermal conductivity of the core does not affect the lifetime of melt production near the surface, which instead depends on the mantle viscosity and the partitioning behavior of the HPEs. However, higher thermal conductivity in the core always leads to shorter-lived and weaker dynamo. Raising or lowering the thermal conductivity of the core by ~25% can reduce or lengthen the predicted dynamo lifetime by several billion years, respectively. The predicted magnetic fields at the surface can likewise change by ~10 mT because thermal conduction acts as a dissipation sink in the core (85). For any value of the thermal conductivity of the core, the siderophile behavior of HPEs makes larger super-Earths relatively more likely to sustain global magnetic fields.

Caveats and priorities for future studies

We designed our thermal evolution models to illustrate the firstorder effects of siderophile HPEs on the evolution of super-Earth exoplanets. This approach, following many previous studies, necessarily embraced several limitations, including but not limited to the following:

- 1) Our models were parametrized and one-dimensional. Mantle convection is intrinsically three-dimensional (3D), featuring latitudinal and longitudinal variations in temperature, composition, and other properties. The scaling laws for stagnant-lid convection have been benchmarked to 3D models, but 3D models could still capture important aspects of planetary evolution that are not illustrated here (50).
- 2) Our models assumed a constant surface temperature and thus only one mode of mantle convection. Stagnant-lid convection has been considered the most natural mode of mantle convection for planets with surfaces that are too hot for stable liquid water. However, the nearest such planet (Venus) may operate in a different mode of mantle convection facilitated by intrusive magmatism (93). Real planets also have atmospheres that evolve in response to stellar evolution and mantle degassing. Climatic shifts can cause the regime of mantle convection to change, plausibly more than once during a planet's lifetime (94, 95). Fully coupled models of atmosphere-surface-mantle-core evolution would be critical to studies that attempt to reproduce the histories of individual planets.
- 3) Studying habitable worlds would require more complicated models, which would describe the atmosphere-surface-interior cycling of key elements such as hydrogen, water, carbon, and sulfur in detail (90, 96). Habitable planets may feature a plate tectonic-like regime of mantle convection, including analogues to both the oceanic and continental crust. Modeling the influence of a planetary magnetic field on surface habitability is also complex and likely varies based on the type of parent star and the planetary orbit (97–99).
- 4) Our models do not include a BMO. Most studies assume that planetary mantles solidify from the bottom up. However, the mantles of Earth-sized and larger planets may crystallize from the center outward. The surficial magma ocean would solidify within ~10 to 100 Myr, depending on the properties of any overlying atmosphere (73). The BMO would remain molten for billions of years (74) because the overlying solid mantle acts as a thermal blanket, and the neighboring core serves as a heat sink. Notably, molten silicates become electrically conductive at extreme pressures and temperatures, meaning that BMOs in super-Earths could host dynamos (62), as proposed for Earth's ancient BMO (100, 101). One would expect substantial amounts of chemical exchange, including of HPEs, between the core and the BMO across the liquid-liquid interface (102).

These limitations are opportunities for future research. Regardless of the model used, the partitioning behavior of HPEs may markedly influence the thermal evolution of terrestrial exoplanets. For example, many previous efforts have ignored the cooling of the core entirely, assuming instead that super-Earths have mantles that are only internally heated (82, 90). Our results imply that this foundational assumption is incorrect for larger planets and that a new foundation should be built for sophisticated models of terrestrial exoplanets, including potentially habitable super-Earths.

Supplementary Materials

This PDF file includes: Figs. S1 to S19 Tables S1 to S7

REFERENCES AND NOTES

- D. Valencia, D. D. Sasselov, R. J. O'Connell, Radius and structure models of the first super-earth planet. Astrophys. J. 656, 545–551 (2007).
- J. J. Fortney, M. S. Marley, J. W. Barnes, Planetary radii across five orders of magnitude in mass and stellar insolation: Application to transits. Astrophys. J. 659, 1661–1672 (2007).
- D. Charbonneau, Z. K. Berta, J. Irwin, C. J. Burke, P. Nutzman, L. A. Buchhave, C. Lovis, X. Bonfils, D. W. Latham, S. Udry, R. A. Murray-Clay, M. J. Holman, E. E. Falco, J. N. Winn, D. Queloz, F. Pepe, M. Mayor, X. Delfosse, T. Forveille, A super-Earth transiting a nearby low-mass star. *Nature* 462, 891–894 (2009).
- L. Kaltenegger, How to characterize habitable worlds and signs of life. Annu. Rev. Astron. Astrophys. 55, 433–485 (2017).
- A. Shahar, P. Driscoll, A. Weinberger, G. Cody, What makes a planet habitable? Science 364, 434–435 (2019).
- 6. S. Seager, Exoplanet habitability. Science 340, 577–581 (2013).
- J. F. Kasting, D. Catling, Evolution of a habitable planet. Annu. Rev. Astron. Astrophys. 41, 429–463 (2003).
- C. T. Unterborn, B. J. Foley, S. J. Desch, P. A. Young, G. Vance, L. Chiffelle, S. R. Kane, Mantle degassing lifetimes through galactic time and the maximum age stagnant-lid rocky exoplanets can support temperate climates. *Astrophys. J. Lett.* 930, L6 (2022).
- P. E. Driscoll, "Planetary interiors, magnetic fields, and habitability" in Handbook of Exoplanets, H. J. Deeg, J. A. Belmonte, Eds. (Springer International Publishing, 2018), pp. 2917–2935.
- D. J. Stevenson, T. Spohn, G. Schubert, Magnetism and thermal evolution of the terrestrial planets. *Icarus* 54, 466–489 (1983).
- E. S. Kite, M. Manga, E. Gaidos, Geodynamics and rate of volcanism on massive Earth-like planets. Astrophys. J. 700, 1732–1749 (2009).
- L. Noack, A. Rivoldini, T. Van Hoolst, Volcanism and outgassing of stagnant-lid planets: Implications for the habitable zone. *Phys. Earth Planet. Inter.* 269, 40–57 (2017).
- N. Tosi, M. Godolt, B. Stracke, T. Ruedas, J. L. Grenfell, D. Honing, A. Nikolaou, A. C. Plesa, D. Breuer, T. Spohn, The habitability of a stagnant-lid Earth. *Astron. Astrophys.* 605, A71 (2017)
- C. Dorn, L. Noack, A. B. Rozel, Outgassing on stagnant-lid super-Earths. Astron. Astrophys. 614. A18 (2018).
- E. S. Kite, M. N. Barnett, Exoplanet secondary atmosphere loss and revival. Proc. Natl. Acad. Sci. U.S.A. 117, 18264–18271 (2020).
- E. Gaidos, C. P. Conrad, M. Manga, J. Hernlund, Thermodynamic limits on magnetodynamos in rocky exoplanets. Astrophys. J. 718, 596–609 (2010).
- C. Tachinami, H. Senshu, S. Ida, Thermal evolution and lifetime of intrinsic magnetic fields of super-Earths in habitable zones. Astrophys. J. 726, 70 (2011).
- P. Driscoll, P. Olson, Optimal dynamos in the cores of terrestrial exoplanets: Magnetic field generation and detectability. *Icarus* 213, 12–23 (2011).
- J. van Summeren, E. Gaidos, C. P. Conrad, Magnetodynamo lifetimes for rocky, Earth-mass exoplanets with contrasting mantle convection regimes. *J. Geophys. Res. Planets* 118, 938–951 (2013).
- A. Boujibar, P. Driscoll, Y. Fei, Super-Earth internal structures and initial thermal states. J. Geophys. Res. Planets 125, e2019JE006124 (2020).
- R. G. Kraus, R. J. Hemley, S. J. Ali, J. L. Belof, L. X. Benedict, J. Bernier, D. Braun, R. E. Cohen, G. W. Collins, F. Coppari, M. P. Desjarlais, D. Fratanduono, S. Hamel, A. Krygier, A. Lazicki, J. McNaney, M. Millot, P. C. Myint, M. G. Newman, J. R. Rygg, D. M. Sterbentz, S. T. Stewart, L. Stixrude, D. C. Swift, C. Wehrenberg, J. H. Eggert, Measuring the melting curve of iron at super-Earth core conditions. Science 375, 202–205 (2022).
- B. J. Foley, C. Houser, L. Noack, N. Tosi, in *Planetary Diversity* (IOP Publishing, 2020), pp. 4-1-4-60.
- C. O'Neill, H. S. C. O'Neill, A. M. Jellinek, On the distribution and variation of radioactive heat producing elements within meteorites, the Earth, and planets. Space Sci. Rev. 216, 1–27 (2020).
- C. Jaupart, S. Labrosse, F. Lucazeau, J.-C. Mareschal, Temperatures, heat, and energy in the mantle of the Earth in *Treatise on Geophysics* S. Gerald, Ed. (Elsevier, 2015), pp. 223–270.
- A. Corgne, S. Keshav, Y. W. Fei, W. F. McDonough, How much potassium is in the Earth's core? New insights from partitioning experiments. *Earth Planet. Sci. Lett.* 256, 567–576 (2007).
- B. A. Chidester, Z. Rahman, K. Righter, A. J. Campbell, Metal-silicate partitioning of U: Implications for the heat budget of the core and evidence for reduced U in the mantle. Geochim. Cosmochim. Acta 199, 1–12 (2017).
- I. Blanchard, J. Siebert, S. Borensztajn, J. Badro, The solubility of heat-producing elements in Earth's core. Geochem. Perspect. Lett. 5, 1–5 (2017).
- A. Boujibar, M. Habermann, K. Righter, D. K. Ross, K. Pando, M. Righter, B. A. Chidester, L. R. Danielson, U, Th, and K partitioning between metal, silicate, and sulfide and implications for Mercury's structure, volatile content, and radioactive heat production. *Am. Mineral.* 104, 1221–1237 (2019).

- P. Faure, M. A. Bouhifd, M. Boyet, G. Manthilake, V. Clesi, J. L. Devidal, Uranium and thorium partitioning in the bulk silicate Earth and the oxygen content of Earth's core. *Geochim. Cosmochim. Acta* 275, 83–98 (2020).
- B. A. Chidester, S. J. Lock, K. E. Swadba, Z. Rahman, K. Righter, A. J. Campbell, The lithophile element budget of Earth's core. *Geochem. Geophys. Geosyst.* 23, e2021GC009986 (2022).
- Z. H. Xiong, T. Tsuchiya, T. Taniuchi, Ab initio prediction of potassium partitioning into Earth's core. J. Geophys. Res. Solid Earth 123, 6451–6458 (2018).
- A. J. Wilson, M. Pozzo, C. J. Davies, A. M. Walker, D. Alfè, Examining the power supplied to Earth's dynamo by magnesium precipitation and radiogenic heat production. *Phys. Earth Planet. Inter.* 343, 107073 (2023).
- L. Yuan, G. Steinle-Neumann, Possible control of Earth's boron budget by metallic iron. Geophys. Res. Lett. 49, e2021GL096923 (2022).
- L. Yuan, G. Steinle-Neumann, Earth's "missing" chlorine may be in the core. J. Geophys. Res. Solid Earth 129, e2023JB027731 (2024).
- R. Dutta, S. J. Tracy, R. E. Cohen, F. Miozzi, K. Luo, J. Yang, P. C. Burnley, D. Smith, Y. Meng,
 Chariton, V. B. Prakapenka, T. S. Duffy, Ultrahigh-pressure disordered eight-coordinated phase of Mg₂GeO₄: Analogue for super-Earth mantles. *Proc. Natl. Acad. Sci. U.S.A.* 119, e2114424119 (2022).
- N. Ikuta, N. Sakamoto, S. Tagawa, K. Hirose, Y. Tsutsumi, S. Yokoo, H. Yurimoto, Pressure dependence of metal–silicate partitioning explains the mantle phosphorus abundance. Sci. Rep. 14, 1194 (2024).
- L. Stixrude, Melting in super-earths. Philos. Transact. A Math. Phys. Eng. Sci. 372, 20130076 (2014).
- R. A. Fischer, Y. Nakajima, A. J. Campbell, D. J. Frost, D. Harries, F. Langenhorst,
 N. Miyajima, K. Pollok, D. C. Rubie, High pressure metal-silicate partitioning of Ni, Co, V,
 Cr. Si, and O. Geochim. Cosmochim. Acta 167, 177–194 (2015).
- J. Wade, B. J. Wood, Core formation and the oxidation state of the Earth. Earth Planet. Sci. Lett. 236, 78–95 (2005).
- D. C. Rubie, S. A. Jacobson, A. Morbidelli, D. P. O'Brien, E. D. Young, J. de Vries, F. Nimmo, H. Palme, D. J. Frost, Accretion and differentiation of the terrestrial planets with implications for the compositions of early-formed solar system bodies and accretion of water. *Icarus* 248, 89–108 (2015).
- D. C. Rubie, D. J. Frost, U. Mann, Y. Asahara, F. Nimmo, K. Tsuno, P. Kegler, A. Holzheid, H. Palme, Heterogeneous accretion, composition and core-mantle differentiation of the Earth. *Earth Planet. Sci. Lett.* 301, 31–42 (2011).
- J. Siebert, J. Badro, D. Antonangeli, F. J. Ryerson, Terrestrial accretion under oxidizing conditions. Science 339, 1194–1197 (2013).
- B. J. Wood, M. J. Walter, J. Wade, Accretion of the Earth and segregation of its core. Nature 441, 825–833 (2006).
- L. Noack, M. Lasbleis, Parameterisations of interior properties of rocky planets: An investigation of planets with Earth-like compositions but variable iron content. *Astron. Astrophys.* 638, A129 (2020).
- C. H. Blaske, J. G. O'Rourke, Energetic requirements for dynamos in the metallic cores of super-Earth and super-Venus exoplanets. J. Geophys. Res. Planets 126, e2020JE006739 (2021).
- E. A. Frank, B. S. Meyer, S. J. Mojzsis, A radiogenic heating evolution model for cosmochemically Earth-like exoplanets. *Icarus* 243, 274–286 (2014).
- T. Miyagoshi, M. Kameyama, M. Ogawa, Effects of adiabatic compression on thermal convection in super-Earths of various sizes. Earth Planets Space 70, 200 (2018).
- Y. Ricard, T. Alboussière, S. Labrosse, J. Curbelo, F. Dubuffet, Fully compressible convection for planetary mantles. *Geophys. J. Int.* 230, 932–956 (2022).
- J. Korenaga, Urey ratio and the structure and evolution of Earth's mantle. Rev. Geophys. 46. (2008).
- P. J. Tackley, M. Ammann, J. P. Brodholt, D. P. Dobson, D. Valencia, Mantle dynamics in super-Earths: Post-perovskite rheology and self-regulation of viscosity. *Icarus* 225, 50–61 (2013).
- S. I. Karato, Rheological structure of the mantle of a super-Earth: Some insights from mineral physics. *Icarus* 212, 14–23 (2011).
- F. Nimmo, J. Primack, S. M. Faber, E. Ramirez-Ruiz, M. Safarzadeh, Radiogenic heating and its influence on rocky planet dynamos and habitability. *Astrophys. J. Lett.* 903, L37 (2020).
- Y. G. Li, L. Vocadlo, T. Sun, J. P. Brodholt, The Earth's core as a reservoir of water. *Nat. Geosci.* 13, 453–458 (2020).
- D. Alfe, M. J. Gillan, G. D. Price, Ab initiochemical potentials of solid and liquid solutions and the chemistry of the Earth's core. J. Chem. Phys. 116, 7127–7136 (2002).
- M. Pozzo, C. Davies, D. Gubbins, D. Alfe, FeO content of Earth's liquid core. Phys. Rev. X 9, 041018 (2019).
- 56. P. E. Blochl, Projector augmented-wave method. Phys. Rev. B 50, 17953–17979 (1994).
- G. Kresse, D. Joubert, From ultrasoft pseudopotentials to the projector augmented-wave method. *Phys. Rev. B* 59, 1758–1775 (1999).

SCIENCE ADVANCES | RESEARCH ARTICLE

- J. P. Perdew, A. Ruzsinszky, G. I. Csonka, O. A. Vydrov, G. E. Scuseria, L. A. Constantin, X. L. Zhou, K. Burke, Restoring the density-gradient expansion for exchange in solids and surfaces. *Phys. Rev. Lett.* **100**, 136406 (2008).
- G. Kresse, J. Furthmuller, Efficiency of ab-initio total energy calculations for metals and semiconductors using a plane-wave basis set. *Comput. Mater. Sci.* 6, 15–50 (1996).
- F. Wagle, G. Steinle-Neumann, Liquid iron equation of state to the terapascal regime from ab initio simulations. J. Geophys. Res. Solid Earth 124, 3350–3364 (2019).
- T. Sjostrom, S. Crockett, Quantum molecular dynamics of warm dense iron and a five-phase equation of state. *Phys. Rev. E* 97, 053209 (2018).
- F. Soubiran, B. Militzer, Electrical conductivity and magnetic dynamos in magma oceans of Super-Earths. Nat. Commun. 9, 3883 (2018).
- F. González-Cataldo, F. Soubiran, H. Peterson, B. Militzer, Path integral Monte Carlo and density functional molecular dynamics simulations of warm dense MgSiO₃. *Phys. Rev. B* 101, 024107 (2020).
- K. Migdal, A. Yanilkin, Cold and hot uranium in DFT calculations: Investigation by the GTH pseudopotential, PAW, and APW+ lo methods. Comput. Mater. Sci. 199, 110665 (2021).
- J. Whaley-Baldwin, Structures of elemental potassium at terapascal pressures. Phys. Rev. B 107, 024106 (2023).
- N. D. Mermin, Thermal properties of the inhomogeneous electron gas. Phys. Rev. 137, A1441–A1443 (1965).
- 67. Y. G. Li, L. Vocadlo, C. Ballentine, J. P. Brodholt, Primitive noble gases sampled from ocean island basalts cannot be from the Earth's core. *Nat. Commun.* **13**, 3770 (2022).
- W. Liu, Y. Zhang, F. Tissot, G. Avice, Z. Ye, Q. Yin, I/Pu reveals Earth mainly accreted from volatile-poor differentiated planetesimals. Sci. Adv. 9, eadg9213 (2023).
- S. Nosé, A unified formulation of the constant temperature molecular-dynamics methods. J. Chem. Phys. 81, 511–519 (1984).
- F. Dorner, Z. Sukurma, C. Dellago, G. Kresse, Melting Si: Beyond density functional theory. Phys. Rev. Lett. 121, 195701 (2018).
- H. Flyvbjerg, H. G. Petersen, Error estimates on averages of correlated data. J. Chem. Phys. 91, 461–466 (1989).
- F. González-Cataldo, B. Militzer, Ab initio determination of iron melting at terapascal pressures and Super-Earths core crystallization. Phys. Rev. Res. 5, 033194 (2023).
- 73. K. Hamano, Y. Abe, H. Genda, Emergence of two types of terrestrial planet on solidification of magma ocean. *Nature* **497**, 607–610 (2013).
- S. Labrosse, J. W. Hernlund, N. Coltice, A crystallizing dense magma ocean at the base of the Earth's mantle. *Nature* 450, 866–869 (2007).
- V. S. Solomatov, L. N. Moresi, Scaling of time-dependent stagnant lid convection: Application to small-scale convection on Earth and other terrestrial planets. *J. Geophys. Res. Solid Earth* 105, 21795–21817 (2000).
- S. Morris, D. Canright, A boundary-layer analysis of Benard convection in a fluid of strongly temperature-dependent viscosity. *Phys. Earth Planet. Inter.* 36, 355–373 (1984).
- C. C. Reese, V. S. Solomatov, L. N. Moresi, Heat transport efficiency for stagnant lid convection with dislocation viscosity: Application to Mars and Venus. J. Geophys. Res. Planets 103, 13643–13657 (1998).
- C. C. Reese, V. S. Solomatov, L. N. Moresi, Non-Newtonian stagnant lid convection and magmatic Resur facing on Venus. *Icarus* 139, 67–80 (1999).
- J. Korenaga, Scaling of stagnant-lid convection with Arrhenius rheology and the effects of mantle melting. Geophys. J. Int. 179, 154–170 (2009).
- G. Schubert, P. Cassen, R. E. Young, Subsolidus convective cooling histories of terrestrial planets. *Icarus* 38, 192–211 (1979).
- 81. S. Herbert, Large Scale Dynamics of Interacting Particles (Springer-Verlag, 1991).
- B. J. Foley, A. J. Smye, Carbon cycling and habitability of Earth-sized stagnant lid planets. Astrobiology 18, 873–896 (2018).
- 83. J. Korenaga, P. B. Kelemen, W. S. Holbrook, Methods for resolving the origin of large igneous provinces from crustal seismology. *J. Geophys. Res. Solid Earth* **107**, 2178 (2002).
- 84. A. A. Fraeman, J. Korenaga, The influence of mantle melting on the evolution of Mars. *Icarus* **210**, 43–57 (2010).
- S. Labrosse, Thermal evolution of the core with a high thermal conductivity. Phys. Earth Planet. Inter. 247, 36–55 (2015).
- M. Pozzo, C. Davies, D. Gubbins, D. Alfe, Transport properties for liquid silicon-oxygeniron mixtures at Earth's core conditions. *Phys. Rev. B* 87, 014110 (2013).

- M. Pozzo, C. J. Davies, D. Alfe, Towards reconciling experimental and computational determinations of Earth's core thermal conductivity. Earth Planet. Sci. Lett. 584, 117466 (2022).
- G. Schubert, K. M. Soderlund, Planetary magnetic fields: Observations and models. *Phys. Earth Planet. Inter.* 187, 92–108 (2011).
- U. R. Christensen, Dynamo scaling laws and applications to the planets. Space Sci. Rev. 152, 565–590 (2010).
- C. Unterborn, L. Schaefer, S. Krijt, in *Planetary Diversity* (IOP Publishing, 2020), pp. 5-1-5-52.
- M. Landeau, J. Aubert, P. Olson, The signature of inner-core nucleation on the geodynamo. Earth Planet. Sci. Lett. 465, 193–204 (2017).
- M. Landeau, A. Fournier, H. C. Nataf, D. Cebron, N. Schaeffer, Sustaining Earth's magnetic dynamo. Nat. Rev. Earth Environ. 3, 255–269 (2022).
- J. C. Tian, P. J. Tackley, D. L. Lourenco, The tectonics and volcanism of Venus: New modes facilitated by realistic crustal rheology and intrusive magmatism. *Icarus* 399, 115539 (2023)
- 94. C. Gillmann, P. Tackley, Atmosphere-mantle coupling and feedbacks on Venus. J. Geophys. Res. Planets 119, 1189–1217 (2014).
- M. B. Weller, W. S. Kiefer, The physics of changing tectonic regimes: Implications for the temporal evolution of mantle convection and the thermal history of Venus. J. Geophys. Res. Planets 125, e2019JE005960 (2020).
- C. Dorn, K. Mosegaard, S. L. Grimm, Y. Alibert, Interior characterization in multiplanetary systems: TRAPPIST-1. Astrophys. J. 865, 20 (2018).
- H. Egan, R. Jarvinen, Y. J. Ma, D. Brain, Planetary magnetic field control of ion escape from weakly magnetized planets. *Mon. Not. R. Astron. Soc.* 488, 2108–2120 (2019)
- R. Sakata, K. Seki, S. Sakai, N. Terada, H. Shinagawa, T. Tanaka, Effects of an intrinsic magnetic field on ion loss from ancient Mars based on multispecies MHD simulations. *J. Geophys. Res. Space Physics* 125, e2019JA026945 (2020).
- C. F. Dong, M. Jin, M. Lingam, Atmospheric escape from TOI-700 d: Venus versus Earth analogs. Astrophys. J. Lett. 896, L24 (2020).
- L. Stixrude, R. Scipioni, M. P. Desjarlais, A silicate dynamo in the early Earth. Nat. Commun. 11. 935 (2020).
- N. A. Blanc, D. R. Stegman, L. B. Ziegler, Thermal and magnetic evolution of a crystallizing basal magma ocean in Earth's mantle. *Earth Planet. Sci. Lett.* 534, 116085 (2020)
- C. J. Davies, M. Pozzo, D. Gubbins, D. Alfe, Transfer of oxygen to Earth's core from a long-lived magma ocean. Earth Planet. Sci. Lett. 538, 116208 (2020).
- 103. U. Mann, D. J. Frost, D. C. Rubie, H. Becker, A. Audetat, Partitioning of Ru, Rh, Pd, Re, Ir and Pt between liquid metal and silicate at high pressures and high temperatures -Implications for the origin of highly siderophile element concentrations in the Earth's mantle. Geochim. Cosmochim. Acta 84, 593–613 (2012).

Acknowledgments

Funding: This work was supported by the National Science Foundation, grant EAR- 2242946 (J.D.); the NASA'S Exoplanet Research Program, grant 80NSSC23K0265 (J.G.O.); the Heising-Simons Foundation, grant 2022-3940 (J.G.O.). Author contributions:

Conceptualization: J.D. and J.G.O. Investigation: H.L. and J.G.O. Methodology: H.L., J.G.O., and J.D. Resources: H.L. and J.D. Funding acquisition: J.D. Data curation: H.L. Validation: H.L. and J.D. Formal analysis: H.L. Software: H.L. and J.G.O. Visualization: H.L. and J.G.O. Supervision: J.D. Project administration: J.D. Writing—original draft: H.L. and J.G.O. Writing—review and editing: H.L., J.G.O., and J.D. Competing interests: The authors declare that they have no competing interests. Data and materials availability: All data needed to evaluate the conclusions in the paper are present in the paper and/or the Supplementary Materials. Examples of raw molecular dynamics simulation outputs and MATLAB code for performing thermal evolution are publicly available from figshare (https://dx.doi.org/10.6084/m9. figshare.25872553). The Vienna Ab initio Simulation Package (VASP) is a proprietary software available for purchase at www.vasp.at/.

Submitted 19 February 2024 Accepted 9 August 2024 Published 13 September 2024 10.1126/sciadv.ado7603